

A comparative study of subcell optoelectronic properties and energy losses in multijunction solar cells

Sai Meghasena Chavali¹, John Roller¹, Mario Dagenais², Behrang H. Hamadani¹

¹Engineering Laboratory, National Institute of Standards and Technology, Gaithersburg, MD 20899

²Department of Electrical and Computer Engineering, University of Maryland, College Park, Maryland 20742, USA

Abstract

External luminescence quantum yields of subcells within several multijunction solar cells were measured using a calibrated hyperspectral imaging system in absolute electroluminescence mode. The measurements allowed direct comparison of subcell device parameters using the electro-optical reciprocity relationship. In particular, differences in the open circuit voltages or even the shape of the current vs voltage curves under air mass 0 illumination among similar subcells can be correlated with the variations in luminescence yields. One important finding of this work is that electroluminescence measurements can help inform solar cell electrical models such as the two-diode model in terms of better parameter selection. We compare energy losses among the different subcells and discuss how the differences in various loss terms affect the overall device performance. Some strategies to improve the overall solar cell device performance are further discussed as a result of this comparative study.

Keywords: multijunction solar cell; electroluminescence; reciprocity; hyperspectral imaging

1. Introduction

Complex internal device structures of multijunction solar cells (MJSCs), resulting from stacking various lattice-matched active and inactive layers and photonics engineering, create challenges in measuring and understanding the charge carrier transport phenomena in these devices [1–3]. Optoelectronic techniques that are routinely used to characterize the performance of MJSCs include current vs voltage (I - V) measurements [2,4], light and voltage bias dependent external quantum efficiency (EQE) measurements [5–7] and electroluminescence (EL) measurements [8,9]. Even though these characterization methods appear independent of each other, a small but expanding body of work in recent years has shown that they are indeed inter-related through the electro-optical reciprocity relationship [10–12].

In particular, it has been demonstrated that EL measurements of solar cells, and their connection to the EQE of the cells through the reciprocity relationship, provide important insight into recombination losses in solar cells [11–15]. Most EL measurements are presented in relative form, instead of in absolute units of photon flux, since calibration of equipment can be challenging. However, when EL is performed as an absolute measurement, it becomes a very powerful tool for determining the external radiative emission rates in solar cells, leading to the computation of the external luminescence quantum yield, Y_{ext} , which is the ratio of output photons to input electrons. This important device parameter is related to the internal luminescence yield but also incorporates the probability of photon re-absorption and re-emission events inside the device. It has been shown that in order to approach the Shockley-Queisser (SQ) limit of power conversion efficiency, Y_{ext} needs to approach unity [16,17].

Recently, absolute EL measurements, combined with other data such as subcell EQEs, have been used to compute device-related energy losses for each of the subcells in a multijunction solar cell

J_{inj} and compare the emission data of similar subcells to understand how the luminescence physics can explain differences in device performance. Hyperspectral imaging is a technique that combines spectroscopy and imaging to obtain a spectrum for each pixel in the image of a sample. The result of hyperspectral imaging is a 3D data cube. To the best of our knowledge, this is the first work of its kind where every pixel of an emission image is calibrated to show the absolute photon flux per energy with a 2 nm spectral scanning. In particular, we show that EL emission rates can be used to guide a two-diode I - V curve model to predict all the subcell's individual I - V curves. Finally, we present the computed energy losses for all the subcells of each device and describe potential factors such as the role of nonradiative recombination in influencing each cell's performance parameters.

2. Experimental Details

The measurement results presented in this work are obtained from three different multijunction solar cells labeled here as D1, D2 and D3 obtained from three different manufacturers. Device D1 is a triple junction solar cell [19] consisting of active layers GaInP/GaAs/GaInNAs and devices D2 and D3 are both of the type GaInP/GaAs/Ge but were fabricated by two different manufacturers. Throughout this paper, we will sometimes refer to any GaInP subcell as the *top* subcell, any GaAs subcell as the *middle* subcell and either the GaInNAs or Ge as the *bottom* subcell in their respective devices. Therefore, across all three devices, the top two subcells are nominally similar. The subcell GaInNAs is a dilute nitride alloy with a band gap energy of 0.93 eV and is better current-matched to the top and middle subcells in D1 under AM0. The Ge subcell, however, is not current-matched to the top two subcells within the device. D1, D2 and D3 have device active areas of 0.988 cm², 0.818 cm² and 2.27 cm², respectively.

EL measurements were performed using the Grand-EOS hyperspectral wide-field imaging system by Photon ETC [20–22] in the LED mode of the device operation. In the LED mode, current is injected into the device from the contacts in the direction of the forward bias voltage. Hyperspectral imaging provides both spatial and spectral information, in high resolution, all within a convenient image cube. An image cube contains an image of the sample for each acquired wavelength. The spectral emission profiles from an entire 20 mm × 20 mm wide field of view were obtained at several injection currents supplied by a source-measure unit. In the spectral region of 400 nm to 1000 nm, image cubes were collected at 2 nm intervals with a visible-near infrared (VIS-NIR) camera for both the top and middle subcells. For the bottom D1 subcell (GaInNAs), a short-wave infrared (SWIR) camera is used for signal detection in the spectral range of 1000 nm to 1400 nm at 10 nm intervals. The Ge bottom subcell EL emission in D2 and D3 (\approx 1800 nm peak) falls outside the sensitivity of the SWIR camera, therefore, no EL data could be measured for the Ge bottom subcells. However, we were still able to learn substantial information regarding the Ge subcells through both the EQE measurements and I - V curve modeling as explained in detail later. Spectral resolution of the system is better than 2 nm in the VIS-NIR region and under 4 nm in the

SWIR region. Acquisition of an image cube typically takes about three to five minutes at moderate to high current densities and longer for low current densities since a longer integration time (> 1 s) will be needed. Device temperature was fixed at 25 °C by placing the cells on a temperature controlled stage. Uncertainty of reported emission rates obtained from direct EL measurements is estimated to be around 10 % or less.

EQE measurements were performed with a monochromator-based differential spectral responsivity system in the spectral range of 280 nm to 1800 nm with appropriate light and voltage bias application to isolate each subcell's EQE response [5,23]. Finally, I - V curve measurements were performed with a custom-designed, multizone solar simulator under AM0 illumination conditions at 25 °C. Appropriate iso-type reference solar cells, which have similar structures to the multijunction cells but with only one electrically active subcell, were used for spectral mismatch calculations to determine and adjust the illumination intensity for each subcell prior to performing the cell's I - V sweep. I - V and EQE results are generally accurate to within 3 %.

3. Results and Discussion

The most important aspect of hyperspectral imaging over conventional electroluminescence imaging is that the full spectral information of localized defects or heterogeneities can be obtained from the image cubes. Local spectral emission information could pinpoint the location of defects with radiative transitions that are different than the main free exciton peak or could elucidate where large nonradiative centers or shunts are located and how they affect local voltage or current flow inside the device. However, this work is focused on the mean response of each subcell because our goal is to correlate macro device performance with the mean EL emission of each subcell. Local variations can be elaborately imaged at a single wavelength or a spectral region and are briefly discussed in section 3.2 but a detailed analysis of the spectral effects of the observed features is beyond the scope of this work.

3.1 Calibration of hyperspectral image cube data

The raw hyperspectral image cube obtained from EL measurements of the MJSCs gives EL intensity in counts as a function of wavelength in nm. For our analysis, however, these uncalibrated measurements must be converted to the absolute external radiative emission rate $R_{\text{ext}}(E)$ in units of photons/m²s eV as a function of the photon energy in eV. This task was accomplished through the use of a spectral calibration factor that was determined separately through the process described here. Light from a quartz-tungsten-halogen lamp (QTH) was input into one of the ports of a small integrating sphere and a 4 mm diameter pinhole aperture was placed on another port of the sphere. A NIST-calibrated spectroradiometer was then used to measure the absolute spectral irradiance of the light exiting the pinhole aperture. The spectral irradiance of the QTH pinhole light, $dE_{\text{irr}}(\lambda)/d\lambda$ is shown in Fig.1 and represents an average irradiance value over the entire area of the pinhole. Furthermore, it can be converted from the units $\frac{\text{W}}{\text{m}^2\text{nm}}$ to $\frac{\text{W}}{\text{m}^2\text{eV}}$ using the relationship

$$\left| \frac{dE_{\text{irr}}}{dE_{\text{ph}}} \right| = \left| \frac{dE_{\text{irr}}}{d\lambda} \right| \frac{\lambda}{E_{\text{ph}}}, \quad (1)$$

where E_{ph} is the photon energy in eV and λ is the wavelength in nm. dE_{irr}/dE_{ph} can be converted to a photon emission rate for calibration purposes, R_{cal} by

$$R_{cal} = \frac{dE_{irr}}{dE_{ph}} \frac{\lambda}{hc}, \quad (2)$$

with λ in m, Planck's constant h in $J \cdot s$ and speed of light c in m/s, rendering the units of R_{cal} as

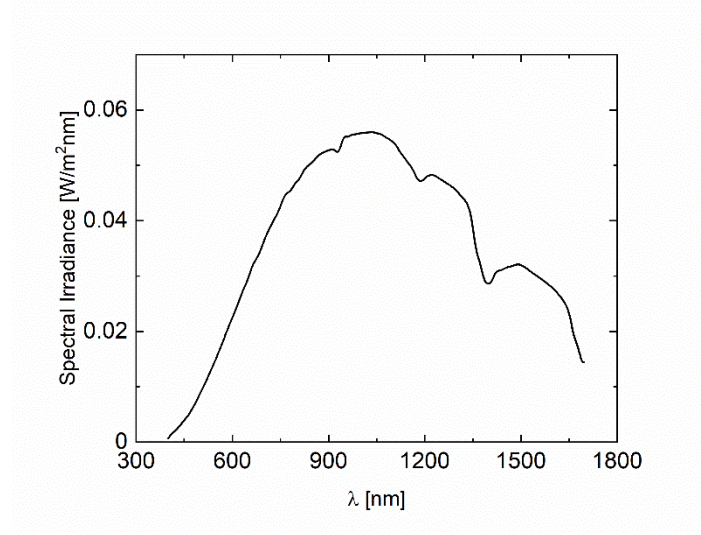


Fig. 1: The spectral irradiance profile of the QTH pinhole aperture used for absolute calibration of the hyperspectral imager.

photons/m²s eV .

Next, we placed the same QTH-illuminated pinhole aperture in the field of view of the hyperspectral imager at the same measurement focal plane as the cells are normally imaged and took a hyperspectral image cube of it over the wavelength range 550 nm to 1600 nm. The spectral calibration factor can be defined as $SCF(\lambda) = R_{cal}(\lambda) / NCR_{QTH}(\lambda)$, where the net counts rate (NCR) is defined as the (total counts – dark counts)/exposure time for the QTH pinhole. The dark counts constitute an image cube where no voltage is applied to the cell (or QTH light is not turned on if performing calibrations) and the total counts is the image cube with applied voltage (or with QTH light on if performing calibrations). The dark subtraction eliminates background noise and other artifacts from the images, leaving behind a clean signal associated with the cell's EL response. Having determined the SCF, subsequent image cube data on solar cells can be converted to absolute emission rates using

$$R_{ext}(\lambda) = NCR_{cell}(\lambda) SCF(\lambda), \quad (3)$$

where NCR_{cell} is the net count rate of the cell under test. This calibration process is only performed once, and the resulting calibration factor is applied to all subsequent EL measurements on solar cells. For this work, we were not concerned with pixel to pixel spectral calibrations since our

analysis was focused on aggregate signals from the entire cell area. However, this calibration process can be applied to all image pixels if the light source standard, i.e., the pinole aperture, has a uniform emission profile across the camera's field of view.

3.2 EL images

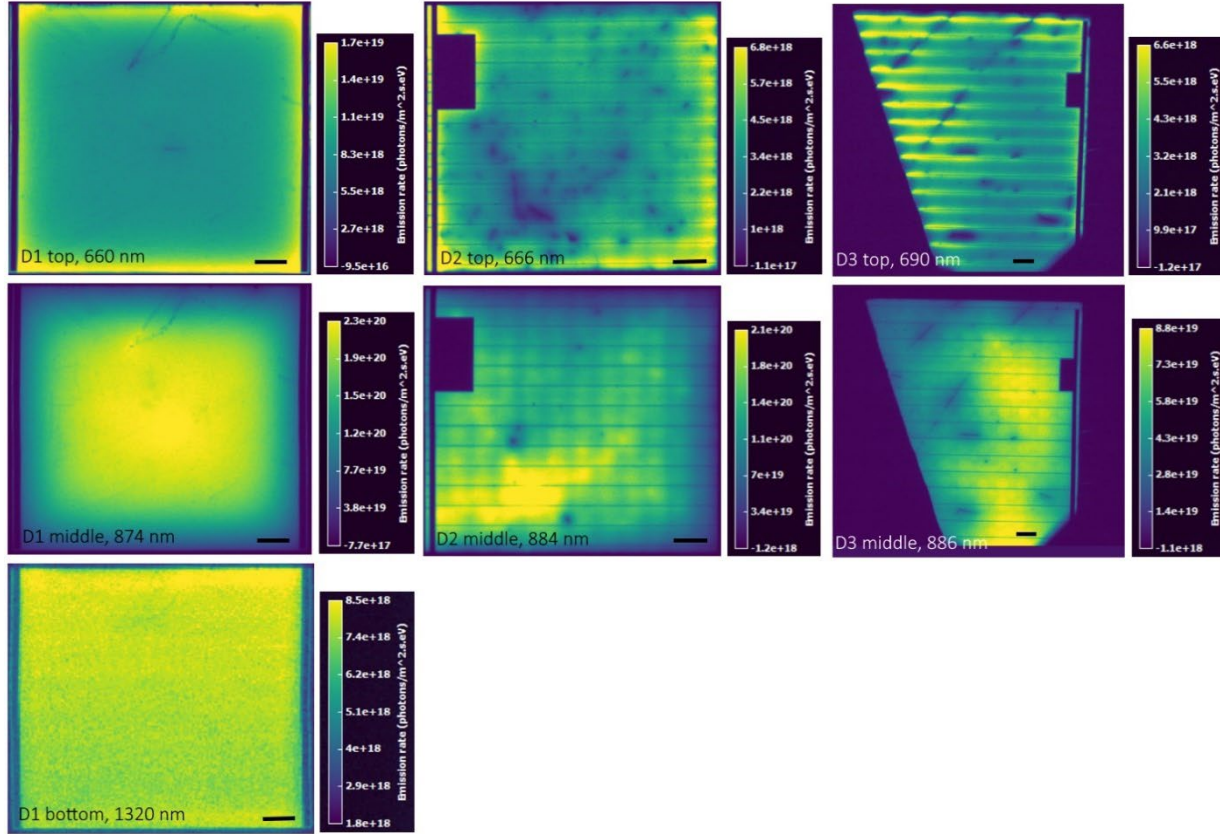


Fig. 2: Absolute hyperspectral EL images of measured subcells at similar current densities for wavelengths labeled for each image. Bottom subcell measurements for devices D2 and D3 are beyond the sensitivity of our instrument. Current densities are: 20.2 mA/cm² for D1 top and D1 middle, 177 mA/cm² for D1 bottom, 18.3 mA/cm² for D2 top and middle, and 19.8 mA/cm² for D3 top and middle. The scale bar in each image is 1 mm.

EL image cubes were obtained on all three multijunction solar cells as a function of injection current, J_{inj} , over the emission spectral region of each subcell, except for the bottom subcell (Ge) in D2 and D3 cells as mentioned earlier. Fig. 2 shows an example of such a series of images, after calibration, at fixed wavelengths corresponding to the peak of the EL emission curve for each subcell. D1 is rectangular in shape, with a thin contact pad on one edge for wire bonding to the cell (not visible in this image) and contains no gridline electrodes on top. D2 has a large contact pad on the top left (dark blue) for wire bonding and has gridlines all across the top surface. D3 is significantly larger than the other two and has an irregular shape with a contact pad on the top right and gridlines all across its top surface. The color scalebar for each image is independent of another image. Significant EL emission heterogeneity can be observed for each subcell, particularly in devices D2 and D3 where localized variations are notable. Darker spots correspond to locations of

defects where either significant nonradiative recombination reduces the radiative signal or physical defects block or scatter the emitted light, preventing it from reaching the camera.

Comparing D1 top and middle images, higher emission from the edges of the top subcell corresponds to lower emission from the edges of the middle subcell. Similar trends can be seen in D2 and D3 top and middle images for *some* of the localized defects where dark spots in the top subcell correspond to brighter spots in the middle, though the bright spots appear somewhat blurry. It has been suggested that inhomogeneous emission from the top subcell, which results in local voltage variations in that material, will have to be balanced out by opposite (but similar) voltage variations in the middle subcell over the same spatial locations [24]. Therefore, lower emission (or voltage) regions in the top cell would then result in higher emission/voltage region from the middle subcell as observed here. Some of the other defects that appear dark in both D2 and D3 are likely surface damage or material defects in one or both subcells. Surface damage, such as small scratch lines, can affect either the top or all layers depending on the depth of the damage.

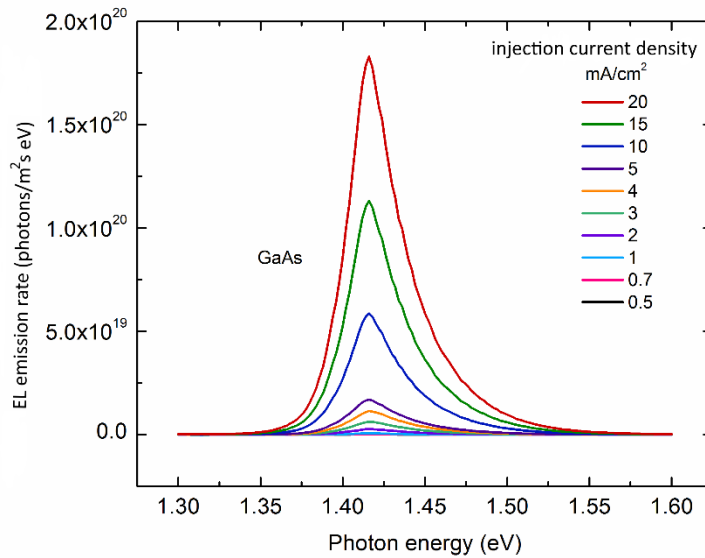


Fig. 3: Absolute EL emission rate spectra of the middle subcell in D1 for various J_{inj} .

Notice that given the same current density, emission rates are higher for the middle GaAs subcells than the top GaInP subcells in all three devices. In the next section, we compare the differences between the EL emission spectra and their magnitudes, focusing on mean device spectra obtained from averaging signals over large areas of the devices through a selection tool available within the software used for the image analysis.

3.3 Absolute EL emission spectra

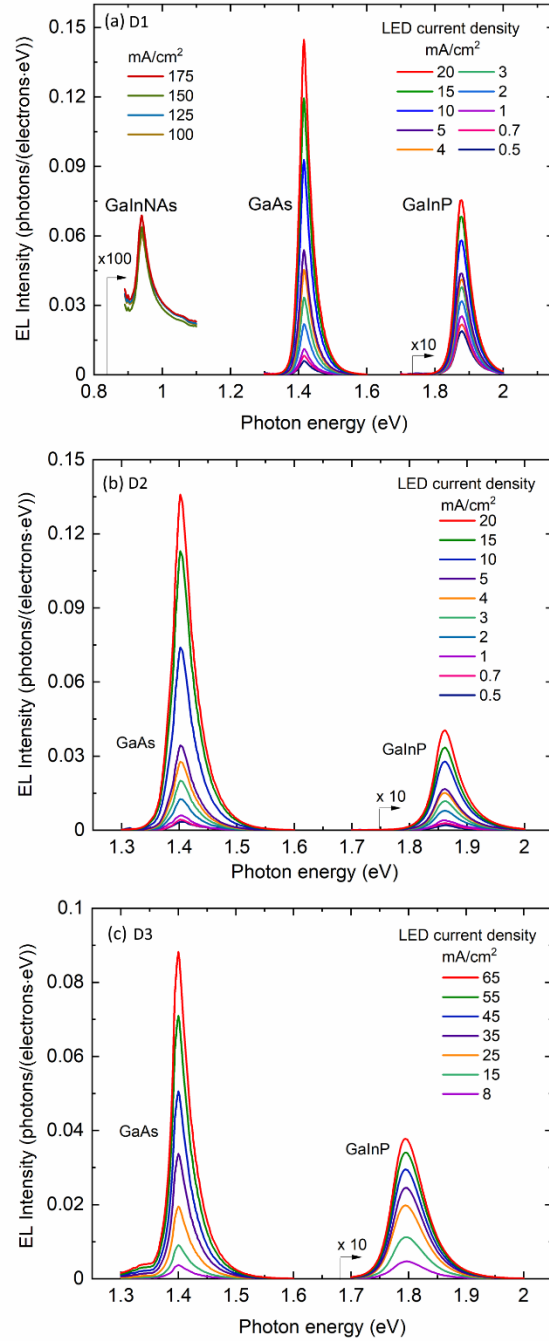


Fig. 4: EL emission rates normalized by the injection current density for all measured subcells in D1 (a), D2 (b) and D3 (c).

Fig. 3 shows the absolute EL emission rate spectra of the middle (GaAs) subcell of the D1 device as a function of E_{ph} or (simply E from here forward) at various J_{inj} levels as labeled inside the plot. Similarly, EL data was obtained for all the other junctions of the three cells except for the Ge junction in D2 and D3. To better understand and compare these results across various devices, these EL photon emission rates can be scaled by J_{inj} and plotted as the ratio $R_{\text{ext}} / J_{\text{inj}}$ as a function of E . Figs. 4 (a-c) show EL intensity of all three multijunction cells plotted in this fashion (in

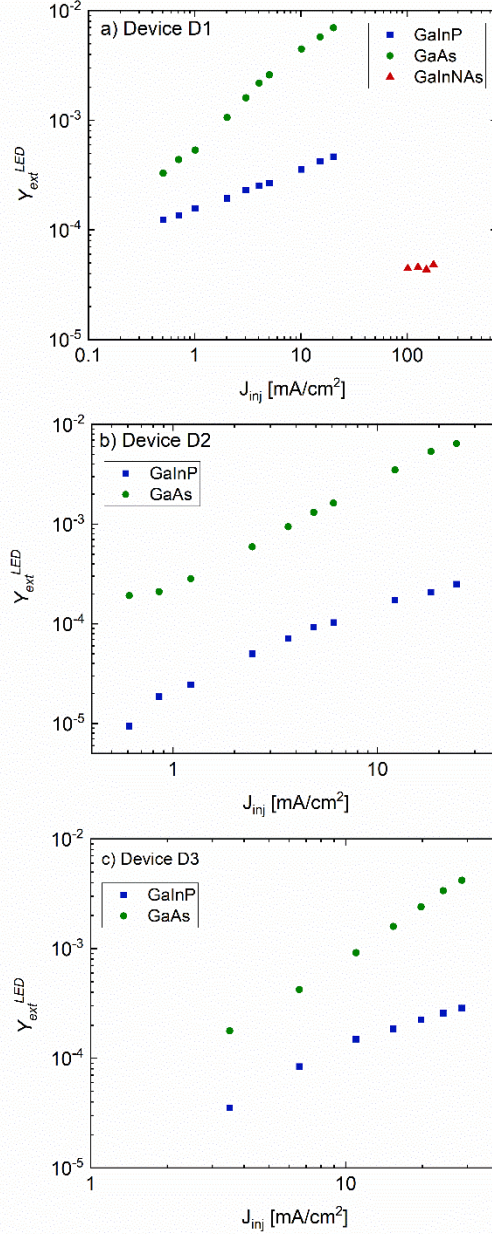


Fig. 5: The external luminescence quantum yields as a function of injection current for all the measured subcells in each device.

units of photons/(electrons·eV)). Notice that the bottom subcell of the D1 cell, the GaInNAs junction, shows a very weak EL emission even at current densities about an order of magnitude higher than those used for the top and the middle subcells. The important observation here is that the scaled EL emission rate curves do not collapse into one curve for each subcell (except for the bottom junction of D1) after this scaling, an indication that the radiative emission rates for these materials are current density dependent. The external luminescence quantum yield for each subcell in LED mode of operation (i.e., under injection current only), $Y_{ext_i}^{LED}$ ($i=1, 2, 3$) is calculated by integrating each curve over all photon energies as defined by

$$Y_{\text{ext}_i}^{\text{LED}} \equiv q \int_{E_{\min}}^{E_{\max}} R_{\text{ext}_i}(E) dE / J_{\text{inj}} = q R_{\text{ext}_i}^{\text{tot}} / J_{\text{inj}}, \quad (4)$$

where q is the electron charge in Coulombs. $Y_{\text{ext}}^{\text{LED}}$ is a unitless quantity representing the fraction of emitted photons per electron injected into the subcell as described earlier.

Table 1: Calculated light generated current for all the subcells based on EQE measurements.

$J_L = qR_{AM0_i}$ (mA/cm ²)	D1	D2	D3
J_{L_1}	18.51	17.45	17.10
J_{L_2}	15.00	17.57	17.27
J_{L_3}	17.51	27.89	30.30

Figs. 5 (a-c) show the log-log plots of $Y_{\text{ext}}^{\text{LED}}$ vs J_{inj} for each subcell. The top and middle junctions for all devices show a power dependence for $Y_{\text{ext}}^{\text{LED}}$ though the power exponent is generally higher for GaAs (0.85 for D1, 1.1 for D2, 1.5 for D3) than for GaInP (0.37 for D1, 0.78 for D2, 0.98 for D3). Also, D3's $Y_{\text{ext}}^{\text{LED}}$ values are lower than D1 and D2, indicating poorer electrical performance for that device as will be discussed later. In general, the higher quantum yields at higher current densities point to increased radiative recombination fraction in these materials because defect-mediated non-radiative recombination tends to saturate at higher injection levels [25,26]. A mathematical treatment of the functional dependence of $Y_{\text{ext}}^{\text{LED}}$ on current density would likely

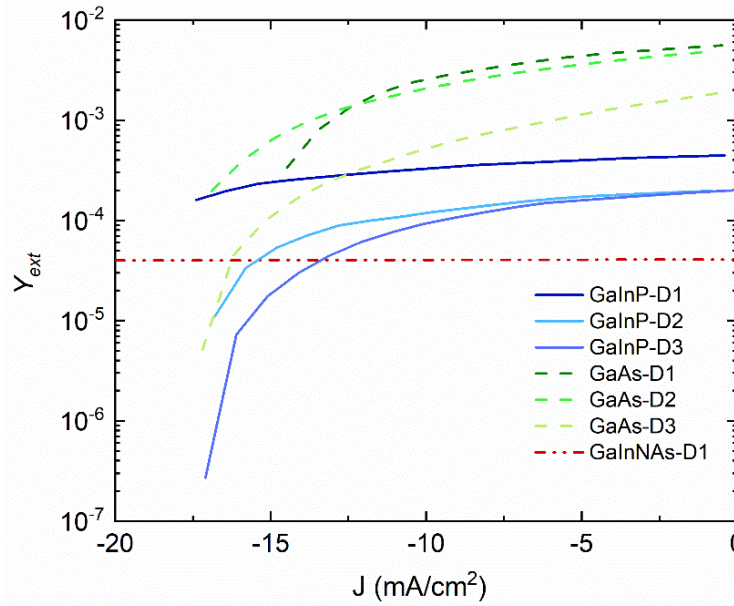


Fig. 6: Calculated external luminescence quantum yields as a function of the subcell current density for all measured subcells.

reveal important information regarding the carrier concentration dependence of radiative and nonradiative (i.e., Shockley-Read-Hall) recombination mechanisms in these devices although this topic is beyond the scope of the current work.

3.4 Calculation of the external luminescence quantum yield in solar cell mode

In the solar cell mode of device operation, there is a combination of photogenerated current and terminal-injected current flowing through the device depending on the applied bias. We are interested in determining the external luminescence yield, Y_{ext} of each subcell as a function of the subcell current density J . A computational approach to translate $Y_{\text{ext}}^{\text{LED}}$ vs J_{inj} measured data to Y_{ext} vs J derived data has been extensively described in Chen et. al. [9] by carefully considering the carrier balance equations for each subcell and associating the $Y_{\text{ext}}^{\text{LED}}$ values for a given J_{inj} to an equivalent subcell current density J that results in the same number of carriers within each subcell.

For cells exposed to the AM0 illumination, the photogenerated current density for each junction can be calculated from $J_{L_i} = qR_{\text{AM0}_i} = q \int EQE_i(E) S_{\text{AM0}} dE$, where R_{AM0_i} is the AM0 generation rate into the junction, EQE_i is the external quantum efficiency of the i th junction, and S_{AM0} is the AM0 photon flux incident on the cell surface, which were calculated from the ASTM E490 air mass 0 tables [27].

Table 1 shows the J_{L_i} values calculated for each subcell of the three MJSCs using the measured EQE curves as shown in Fig. 7. In the carrier balance equations, nonradiative emission rates,

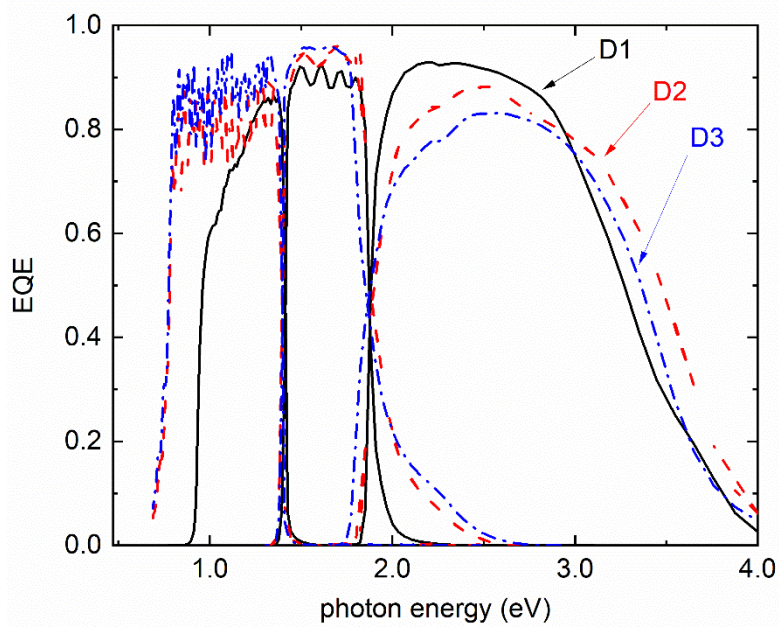


Fig. 7: The external quantum efficiency measurements of the top, middle and bottom subcells within each device.

R_{nr} , and luminescent coupling emission rates R_{LCi} from junction i to $i+1$ are also included and must be properly accounted for. The mathematical treatment, which closely follows that of reference [9] has been extensively described in chapter 3 of reference [28]. Here, we present the results of these extensive computations in Fig. 6 for all measured subcells. Notice that Y_{ext} is now plotted as a function of the subcell operating current J which is negative in this convention. Significant differences in Y_{ext} can be observed among nominally similar subcells, indicating that defect densities and radiative to nonradiative recombination ratios are not the same among the subcells. In particular, the middle junction within the D3 device shows luminescence efficiencies that are lower by a factor of 3 at $J = 0$ which corresponds to the operation of the subcell near its open circuit voltage, V_{oc} . In general, we have observed that in devices with larger density of localized defects, the overall Y_{ext} is lower. These findings help reveal the origin of energy losses within each MJSC, as will be discussed below.

3.5 Subcell J - V curve calculations and modeling

Since electroluminescence is the reciprocal process to the conventional operation of a solar cell, the electro-optical reciprocity relationship can be used to relate the EL emission rates to the EQE and voltage loss across a given subcell of the solar cell. Therefore, absolute EL measurements from the individual subcells within a multijunction cell can serve as a unique way to obtain the individual subcell J - V curves, providing useful information regarding the electrical properties of each junction within the cell stack. The reciprocity relationship states that [9,11]:

$$R_{ext}(E, V) = EQE(E)B(E) \exp\left(\frac{q(V - JAR_s)}{kT}\right) \quad (5)$$

where $B(E) \cong 2\pi E^2 h^{-3} c^{-2} \exp(-E/kT)$ is the spectral photon density of a blackbody, k is Boltzmann's constant, h is Planck's constant, A is the device area, T is the temperature of the junction, c is the speed of light in a vacuum and R_s is the series resistance external to the cell. Solving Eq. 5 for $V(J)$ gives:

$$V_i(J) = \frac{kT}{q} \ln \frac{R_{ext_i}^{tot}(J)}{\langle EQE_i \rangle_{EL} \int_{E_g}^{\infty} B(E) dE} + JAR_s \quad (6)$$

The term $\langle EQE_i \rangle_{EL} = \int EQE_i(E) R_{ext_i}(E) dE / \int R_{ext_i}(E) dE$ is an average EQE term over the EL spectral emission region. Here, the bandgap energies, E_{g_i} were estimated from the inflection point in the long wavelength tail region of the EQE curve for each junction [29,30].

Fig. 8 shows the EL-derived subcell J - V curves of device D1 using Eq. 6. For each subcell, the $R_{ext_i}^{tot}(J)$ term is computed over a range of current densities based on the $Y_{ext}(J)$ derived curves shown in Fig. 6. We note that using this approach, one cannot obtain points along a subcell's entire J - V curve because as we move from the V_{oc} towards V_m and ultimately $V = 0$ along the curve, the difference between the solar cell current J and the light generated current J_L decreases

substantially, meaning that $Y_{\text{ext}}^{\text{LED}}$ must be measured at a very small J_{inj} . Electroluminescence measurements under very low current densities (generally less than $\approx 0.5 \text{ mA/cm}^2$) are very challenging and ultimately run into the detection limit and signal-to-noise ratios of the instruments. The partial J - V curve points for the GaInP and the GaAs junctions plotted in Fig. 8 reflect this fact, but it is even more relevant for the GaInNAs bottom subcell. For this junction, we were only able to calculate a small segment of the J - V curve located far into the forward bias regime (positive currents) past its V_{oc} because the EL measurements were performed with a significantly less sensitive SWIR detection system even under high J_{inj} values.

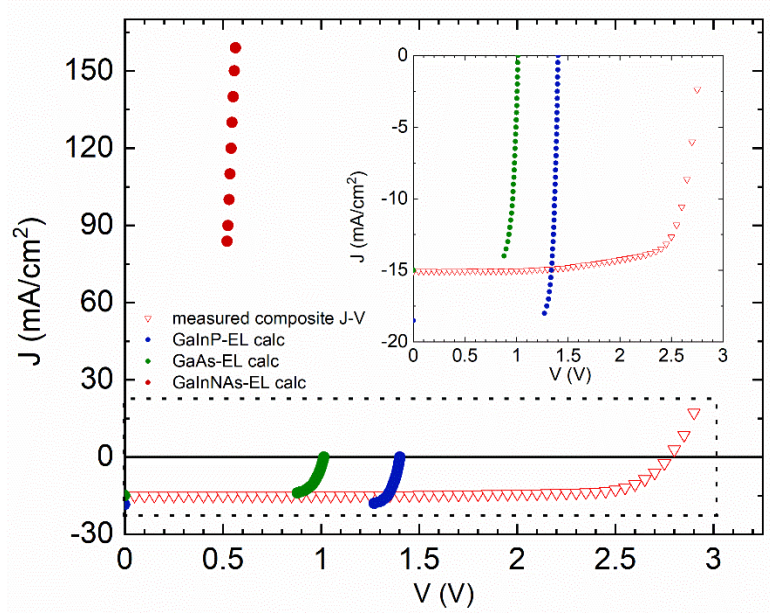


Fig. 8: Reciprocity-derived partial J - V curves (filled symbols) and the measured composite J - V curve (open symbols) under AM0 for D1 and its 3 subcells. The inset magnifies the boxed region shown in the plot for a closer look.

Also shown in Fig. 8 is the composite J - V curve of the D1 multijunction cell (open triangles) measured using a multizone solar simulator under AM0 illumination. With the aid of the composite and partial J - V curves, we can fully reconstruct the subcell J - V curves using a well-accepted equivalent circuit model such as the two-diode model [4]. In this model, the implicit J - V curve for each subcell i can be written in the forward bias direction as:

$$J_i(V) = -J_{L_i} + J_{01_i} \left(\exp \left(\frac{q(V - R_{s_i} A J_i(V))}{k T} \right) - 1 \right) + J_{02_i} \left(\exp \left(\frac{q(V - R_{s_i} A J_i(V))}{n_i k T} \right) - 1 \right) + \frac{V - R_{s_i} A J_i(V)}{R_{sh_i} A} \quad (7)$$

In the reverse bias, the right side of Eq. 7 is multiplied by the factor $1/(1 - (V/V_{bd_i})^{n_{m_i}})$ to account for avalanche breakdown. Here, J_{01_i} is the saturation current density for the quasi-neutral regions, J_{02_i} is the saturation current density for non-radiative mechanisms in the depletion and perimeter regions, n_i is the ideality factor associated with those mechanisms, R_{s_i} is series resistance, R_{sh_i} is the shunt resistance, n_{m_i} is the Miller index and V_{bd_i} is the breakdown voltage. We used Eq. 7 to calculate each subcell's J - V curve such that, 1) the model-calculated J - V curve achieved a reasonably good visual fit to the partial EL-derived J - V curve, and 2) the series sum of the three subcell J - V curves reproduced the measured composite J - V curve for the entire cell. These calculations were performed by varying the parameters J_{01} , J_{02} , and n , while keeping the other model parameters mostly fixed across all devices. Also, the J_{sc} of the composite curve always matched the J_L calculated value for the limiting subcell. The one exception to this modeling approach was the Ge subcell on devices D2 and D3. Since we had no EL-derived J - V curves for that subcell, we simply calculated that subcell's J - V curve such that condition 2 above was satisfied. This calculation would not be very accurate without the EL-derived J - V s of the top and middle subcells as explained below. The model parameters for that junction are consistent with values reported previously [5]. The Ge junction suffers from a low breakdown voltage/shunt resistance and high saturation current densities and therefore shows very nonideal J - V curve behavior.

Table 2: Fit parameters used for the two-diode model calculations with estimated uncertainties. V_{bd} values for Ge subcells are taken from [5].

Device D1	R_s [Ω]	R_{sh} [Ω]	J_L [A/m^2]	J_{01} [A/m^2]	J_{02} [A/m^2]	n	n_m	V_{bd} [V]
Top	0.5 ± 0.3	500 ± 100	185.1 ± 5.5	$5 \times 10^{-22} \pm 1 \times 10^{-22}$	$1 \times 10^{-6} \pm 5 \times 10^{-7}$	3.3 ± 0.1	3	<-10
Middle	0.5 ± 0.3	>5k	150.0 ± 4.5	$9 \times 10^{-16} \pm 1 \times 10^{-16}$	$3 \times 10^{-5} \pm 5 \times 10^{-6}$	2.8 ± 0.1	3	<-10
Bottom	0.5 ± 0.3	45 ± 10	175.1 ± 8.8	$< 1 \times 10^{-5}$	$8 \times 10^{-2} \pm 1 \times 10^{-2}$	2 ± 0.1	3	<-10
Device D2								
Top	0.5 ± 0.3	>5k	174.5 ± 5.2	$9 \times 10^{-22} \pm 1 \times 10^{-22}$	$6 \times 10^{-6} \pm 1 \times 10^{-6}$	3.3 ± 0.1	3	<-10
Middle	0.5 ± 0.3	>5k	175.7 ± 5.3	$7 \times 10^{-16} \pm 2 \times 10^{-16}$	$1 \times 10^{-4} \pm 2 \times 10^{-5}$	2.8 ± 0.1	3	<-10
Bottom	0.5 ± 0.3	45 ± 10	278.9 ± 14.0	$< 10^{-2}$	3.5 ± 0.5	2 ± 0.1	3	-1.8
Device D3								
Top	0.5 ± 0.3	>5k	171.0 ± 5.1	$9 \times 10^{-22} \pm 1 \times 10^{-22}$	$1.8 \times 10^{-5} \pm 1 \times 10^{-16}$	3.25 ± 0.1	3	<-10
Middle	0.5 ± 0.3	>5k	172.7 ± 5.2	$1 \times 10^{-15} \pm 2 \times 10^{-16}$	$2.2 \times 10^{-4} \pm 3 \times 10^{-5}$	2.8 ± 0.1	3	<-10
Bottom	0.5 ± 0.3	45 ± 10	303.0 ± 15.1	$< 10^{-2}$	25 ± 4	1.5 ± 0.1	3	-1.8

Figs. 9 (a-c) show the reciprocity derived partial J - V curves, the modeled subcell and composite J - V curves and the measured composite J - V curves for all three devices. It is important to note that the reciprocity-derived J - V method significantly aides the model-derived J - V calculations by predicting the V_{oc} values of the two GaInP and GaAs subcells and to a lesser degree the curvature of the J - V curve near the maximum operating voltage, V_m . Basically, EL results inform the two-diode model in terms of parameter selection for the J_{01} , J_{02} , and n values. The deviation seen between the two-diode model and the reciprocity-derived J - V curves near the maximum power point (MPP) in D1 could indicate errors in EL measurements of the subcells, particularly in the top subcell, under very low J_{inj} . Overall, the model shows good agreement with data based on the parameters reported in table 2. As long as the EL measurements are accurate, the partial EL-derived J - V curves of the top and middle subcells heavily constrain the model parameters for those

two subcells. Therefore, we are able to predict the Ge subcell J - V , even without EL measurements since the overall composite J - V curve is separately measured.

Comparing the two nominally similar D2 and D3 devices, it is observed that the bottom junction in D3 is a substantial cause of the overall lower device performance, accounting for approximately

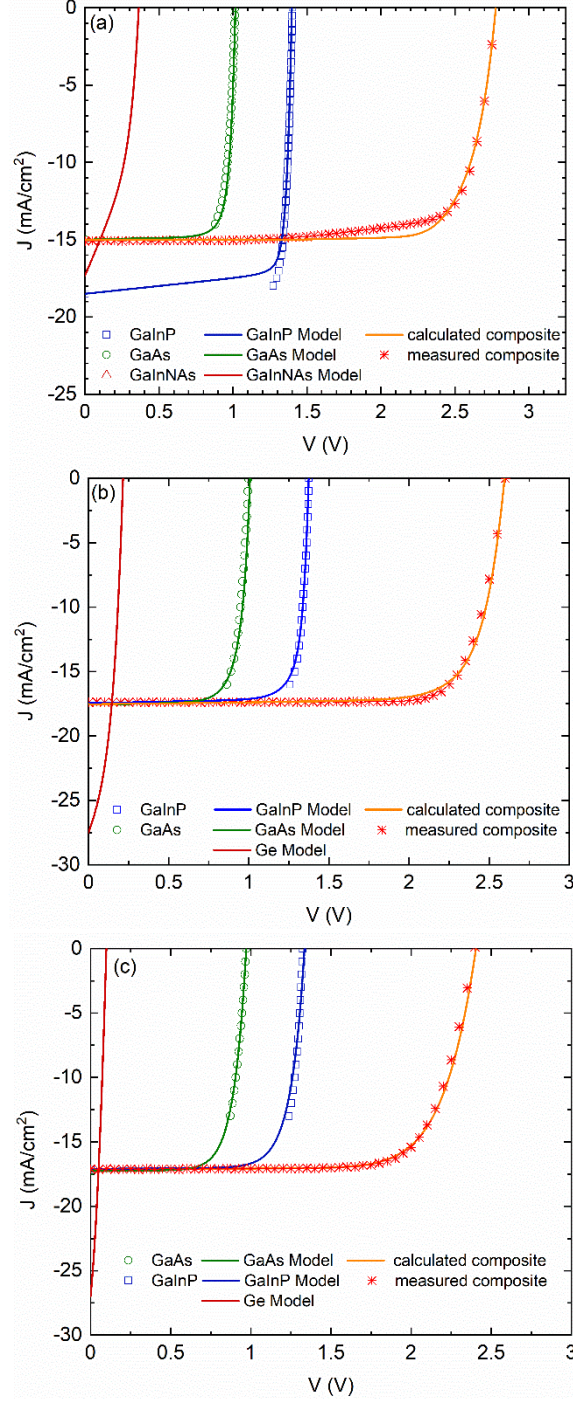


Fig. 9: Two-diode model fits to the reciprocity-derived J - V curves and the composite J - V curve for D1 (a), D2 (b) and D3 (c).

120 mV to 130 mV of the ≈ 200 mV difference between the two devices' composite V_{oc} . Our

measurements and modeling let us determine that an additional ≈ 50 mV in ΔV_{oc} comes from the difference in the two GaInP subcells and another ≈ 25 mV from the GaAs subcells. The lower external luminescence yields of the GaInP and GaAs subcells in D3 reveal slightly lower V_{oc} values for those two subcells compared to the equivalent D2 subcells and these combined differences cause a poorer D3 device performance. In fact, $Y_{ext}(J)$ measurements help explain the differences between the voltages. The voltage penalty from the ideal SQ V_{oc} is given by $kT \ln(Y_{ext})$ [16] and it can be shown that this loss term is directly related to the differences in voltages observed above.

Table 3: Energy loss fractions, normalized by the incident power at device MPP.

D1	AM0	TH	EM	LC	NR	JN	Output Power
Top	0.324	0.069	1.64×10^{-5}	2.01×10^{-4}	0.063	0.054	0.137
Middle	0.180	0.025	6.38×10^{-6}	8.04×10^{-5}	0.011	0.053	0.091
Bottom	0.152	0.033	9.86×10^{-7}	-	0.025	0.080	0.015
TR	0.343	-	-	-	-	-	-
Total	0.999	0.126	2.37×10^{-5}	2.81×10^{-4}	0.099	0.187	0.243
PCE (measured)							0.237
D2							
Top	0.311	0.071	4.96×10^{-7}	6.07×10^{-6}	0.018	0.076	0.143
Middle	0.215	0.035	5.17×10^{-6}	6.51×10^{-5}	0.015	0.066	0.099
Bottom	0.216	0.076	2.41×10^{-6}	-	0.060	0.063	0.018
TR	0.258	-	-	-	-	-	-
Total	0.998	0.181	8.08×10^{-6}	7.12×10^{-5}	0.093	0.205	0.261
PCE (measured)							0.267
D3							
Top	0.301	0.074	1.59×10^{-7}	1.95×10^{-6}	0.017	0.080	0.128
Middle	0.211	0.034	8.26×10^{-7}	1.04×10^{-5}	0.015	0.072	0.090
Bottom	0.235	0.082	2.97×10^{-6}	-	0.073	0.073	0.006
TR	0.254	-	-	-	-	-	-
Total	0.998	0.190	3.95×10^{-6}	1.23×10^{-5}	0.105	0.225	0.225
PCE (measured)							0.227

Table 3 Notes: D1 (GaInP/GaAs/GaInNAs), D2 (GaInP/GaAs/Ge) and D3 (GaInP/GaAs/Ge) are triple junction solar cells by three different manufacturers. Energy loss fractions are normalized by the incident AM0 extraterrestrial irradiance equaling 1366 W/m^2 . TR loss refers to the sum of the below bandgap transmission and surface reflections. TH is the thermalization loss, EM and LC are radiative emission losses into space (EM) or junction below (LC), NR is the non-radiative recombination loss and JN refers to losses at the junction. The output power is the max power produced by each subcell normalized by the incident irradiance and is therefore the power conversion efficiency (PCE).

3.6 Calculating subcell major energy losses

Within the confines of the Detailed Balance model, various energy loss mechanisms can be identified within each subcell of the multijunction solar cell. The most important losses are recombination losses, thermalization (TH) loss, transmission (TR) loss and the junction (JN) loss. Transmission and thermalization losses, which account for incident energy lost to unabsorbed photons and energy lost to electrons thermalizing to the edge of the conduction band, respectively, are computed from the EQE and the incident light's photon flux. Recombination losses, including contributions from both the radiative and non-radiative (NR) recombination processes, can be estimated from the Y_{ext} measurements. The junction loss describes how much energy is lost when a photogenerated charge carrier with an initial energy equal to the band gap energy E_g traverses across a junction experiencing a potential difference V , and is a combination of various losses such as the angular mismatch, Carnot and resistive losses [31].

Table 3 summarizes the major subcell energy losses under AM0 illumination, with each cell operated under the MPP of the MJSC, using the equations outlined in Table IV of Chen et. al. [9]. All the losses and the output power have been normalized to the incident irradiance (1366 W/m^2). Also shown are the computed but negligible radiative emission (EM) and luminescent coupling (LC) losses in order to remain consistent with the Chen precedent. For the Ge subcell calculations, we used the Y_{ext} values reported in [9], which affects only the EM and NR losses. The major loss values reported in Table 3 have the following relative uncertainty values: TH: $\approx 1 \%$, JN: $\approx 1.5 \%$, TR: 1% , NR: $< 0.1 \%$. As a consistency check, we have verified that each row's sum of fractional losses and the subcell fractional output power equal to the fraction of AM0 irradiance over that subcell's absorption region. Furthermore, the sum of all losses including the transmission loss and the output power approximately equal unity. We also calculated the power conversion efficiencies of each cell from the J - V measurements and these numbers agree well with the sum of all three subcell power outputs.

3.7 Device Insights

First, we focus on D1 and D2 results, comparing devices with different bottom subcells. The bottom subcell in D1 has a 0.93 eV band gap compared to the 0.70 eV band gap energy of the Ge subcell in D2. This difference in E_g results in a smaller total TH loss in D1 and an extra 0.055 in fractional AM0 power (out of the total 1). However, this gain comes at the cost of an extra 0.085 in TR losses compared to D2. Lower JN losses compared to D2 help reduce D1's total energy losses but the overall power output for D1 (0.243) is still lower than that of D2 (0.261). Notice that even as the overall NR losses between the two cells are nearly equal, there are substantial differences in individual subcell NR losses. The NR loss partly depends on the difference between the light generated current in each junction and the overall operational current of the composite cell. For D1, the middle subcell is significantly current limiting under AM0, whereas for both D2 and D3, the top and middle subcells are relatively well-matched, with the top subcell's J_L being only slightly lower than those of the middle subcells. The larger mismatch in these currents results in larger NR losses as can be seen for NR values in the top subcell in D1 and the bottom subcell in D2.

Next, we compare D2 and D3 results. These two devices are nominally similar, yet D2 is ≈ 0.04 points more efficient. Comparing the energy losses, we observe that D3 suffers from substantially more NR and JN losses. Both of these losses are largely due to the poor diode behavior of the bottom subcell, but the top and middle subcells also show slightly more JN losses in D3 than in D2. As mentioned earlier, the lower Y_{ext} values of both the top and middle subcells in D3 result in lower V_{oc} values according to the reciprocity relationship. Lower V_{oc} does translate to lower operational voltage values, which will increase the JN losses, but we also observe a softer bending of the J - V curves near the V_m for both the top and middle subcells in D3. This effect is consistent with our measurements showing that the external luminescence efficiency begins to decrease in this region, and does so more rapidly in D3 (see Fig. 6 at $J < -15 \text{ mA/cm}^2$). Therefore, absolute EL measurements, even on two of the three subcells, provide a means to explain subtle differences between nominally similar multijunction solar cells.

All other energy losses listed in Table 3 (i.e., EM, LC) are too small to impact the balance of energy within the subcells as tabulated here. Since TH and TR losses are mostly unavoidable unless

Y_{ext} values that show little dependence on current density will also help increase V_m of the subcells, therefore reducing JN losses as well.

4. Conclusions

Absolute hyperspectral imaging in electroluminescence mode was used to measure the subcell external luminescence quantum yields in several different multijunction solar cells. The system has been uniquely calibrated so that every pixel contains the emission rates at a given photon energy, a major improvement over previous reports. From these measurements, subcell J - V curves, even for Ge subcells with no EL measurements, were constructed. The EL-derived partial J - V curves were instrumental in making informed choices regarding the parameters of the double-diode model used to fully construct all three subcell J - V curves for each device. Additionally, radiative and nonradiative recombination losses were computed and compared against each other to gain more insight into the performance of these devices under AM0 illumination. Some device related differences, such as those in the open circuit voltage among nominally similar subcells can be explained by luminescence efficiencies of the subcells. We computed other major energy losses in these devices to understand the overall balance of energy within each stack and have clearly shown that factors such as higher junction losses and lower radiative efficiency contribute to more degraded performance in a given device.

Acknowledgements

B. H. H would like to thank Dr. Brianna Conrad of NIST for helpful and informative discussions regarding this work and Nicolas Marquez Peraca, currently at Rice University, for setting up the groundwork for these measurements a few years earlier. S. M. Chavali extends her gratitude to Professor Agis Iliadis of the University of Maryland for serving on her thesis committee. Finally, B. H. H. extends his deep gratitude to D. Taner Bilir, formerly of Solar Junction Corporation, for providing some of the materials used in this study and for his unwavering support and enthusiasm regarding this work.

References

- [1] S. Kurtz, J. Geisz, Multijunction solar cells for conversion of concentrated sunlight to electricity, *Opt. Express*. 18 (2010) 73–78. <https://doi.org/10.1364/OE.18.000A73>.
- [2] D.J. Friedman, J.F. Geisz, M.A. Steiner, Analysis of multijunction solar cell current-voltage characteristics in the presence of luminescent coupling, *IEEE J. Photovoltaics*. 3 (2013) 1429–1436. <https://doi.org/10.1109/JPHOTOV.2013.2275189>.
- [3] J.F. Geisz, M.A. Steiner, I. Garcia, R.M. France, W.E. McMahon, C.R. Osterwald, D.J. Friedman, Generalized Optoelectronic Model of Series-Connected Multijunction Solar Cells, *IEEE J. Photovoltaics*. 5 (2015) 1827–1839. <https://doi.org/10.1109/JPHOTOV.2015.2478072>.
- [4] M.A. Steiner, J.F. Geisz, Non-linear luminescent coupling in series-connected multijunction solar cells, *Appl. Phys. Lett.* 100 (2012) 1–5. <https://doi.org/10.1063/1.4729827>.
- [5] J.P. Babaro, K.G. West, B.H. Hamadani, Spectral response measurements of multijunction solar cells with low shunt resistance and breakdown voltages, *Energy Sci. Eng.* 4 (2016) 372–382. <https://doi.org/10.1002/ese3.141>.
- [6] J. Li, S. Member, Y. Zhang, S. Member, Elimination of Artifacts in External Quantum Efficiency Measurements for Multijunction Solar Cells Using a Pulsed Light Bias, *IEEE J. Photovoltaics*. 3 (2013) 364–369.
- [7] N.M. Peraca, D.T. Bilir, B.H. Hamadani, Frequency response of the external quantum efficiency in multijunction solar cells, *Opt. Express*. 25 (2017) A709. <https://doi.org/10.1364/oe.25.00a709>.
- [8] S. Roensch, R. Hoheisel, F. Dimroth, A.W. Bett, Subcell I-V characteristic analysis of GaInP/GaInAs/Ge solar cells using electroluminescence measurements, *Appl. Phys. Lett.* 98 (2011) 251113. <https://doi.org/10.1063/1.3601472>.
- [9] S. Chen, L. Zhu, M. Yoshita, T. Mochizuki, C. Kim, H. Akiyama, M. Imaizumi, Y. Kanemitsu, Thorough subcells diagnosis in a multi-junction solar cell via absolute electroluminescence-efficiency measurements, *Sci. Rep.* 5 (2015) 7836. <https://doi.org/10.1038/srep07836>.
- [10] U. Rau, Superposition and Reciprocity in the Electroluminescence and Photoluminescence of Solar Cells, *IEEE J. Photovoltaics*. 2 (2012) 169–172. <https://doi.org/10.1109/JPHOTOV.2011.2179018>.
- [11] T. Kirchartz, U. Rau, Detailed balance and reciprocity in solar cells, *Phys. Status Solidi*. 205 (2008) 2737–2751. <https://doi.org/10.1002/pssa.200880458>.
- [12] T. Kirchartz, A. Helbig, W. Reetz, M. Reuter, J.H. Werner, U. Rau, Reciprocity between electroluminescence and quantum efficiency used for the characterization of silicon solar cells, *Prog. Photovoltaics Res. Appl.* 17 (2009) 394–402. <https://doi.org/10.1002/pip.895>.
- [13] R. Hoheisel, D. Scheiman, S. Messenger, P. Jenkins, R. Walters, Detailed Characterization of the Radiation Response of Multijunction Solar Cells Using Electroluminescence Measurements, *IEEE Trans. Nucl. Sci.* 62 (2015) 2894–2898. <https://doi.org/10.1109/TNS.2015.2498838>.
- [14] A. Delamarre, L. Lombez, J.F. Guillemoles, Characterization of solar cells using electroluminescence and photoluminescence hyperspectral images, in: A. Freundlich, J.-F.F. Guillemoles (Eds.), *Physics, Simulation, Photonic Eng. Photovolt. Devices*, 2012: p. 825614. <https://doi.org/10.1117/12.906859>.
- [15] T. Kirchartz, V. Huhn, A. Gerber, B.E. Pieters, U. Rau, Electroluminescence Analysis of Solar Cells and Solar Modules, in: *Adv. Charact. Tech. Thin Film Sol. Cells*, Wiley-VCH Verlag GmbH & Co. KGaA, Weinheim, Germany, 2016: pp. 71–92. <https://doi.org/10.1002/9783527699025.ch3>.
- [16] O.D. Miller, E. Yablonovitch, S.R. Kurtz, Strong Internal and External Luminescence as Solar Cells Approach the Shockley–Queisser Limit, *IEEE J. Photovoltaics*. 2 (2012) 303–311. <https://doi.org/10.1109/JPHOTOV.2012.2198434>.

- [17] E. Yablonovitch, O.D. Miller, S.R. Kurtz, The opto-electronic physics that broke the efficiency limit in solar cells, in: 2012 38th IEEE Photovolt. Spec. Conf., IEEE, 2012: pp. 001556–001559. <https://doi.org/10.1109/PVSC.2012.6317891>.
- [18] X. Hu, T. Chen, J. Xue, G. Weng, S. Chen, H. Akiyama, Z. Zhu, Absolute Electroluminescence Imaging Diagnosis of GaAs Thin-Film Solar Cells, *IEEE Photonics J.* 9 (2017) 1–9. <https://doi.org/10.1109/JPHOT.2017.2731800>.
- [19] R. Jones-Albertus, E. Becker, R. Bergner, T. Bilir, D. Derkacs, O. Fidaner, D. Jory, T. Liu, E. Lucow, P. Misra, E. Pickett, F. Suarez, A. Sukiasyan, T. Sun, L. Zhang, V. Sabnis, M. Wiemer, H. Yuen, Using dilute nitrides to achieve record solar cell efficiencies, in: *Mater. Res. Soc. Symp. Proc.*, 2013: pp. 161–166. <https://doi.org/10.1557/opl.2013.656>.
- [20] E. Gaufrès, S. Marcet, V. Aymong, N.Y.-W. Tang, A. Favron, F. Thouin, C. Allard, D. Rioux, N. Cottenye, M. Verhaegen, R. Martel, Hyperspectral Raman imaging using Bragg tunable filters of graphene and other low-dimensional materials, *J. Raman Spectrosc.* 49 (2018) 174–182. <https://doi.org/10.1002/jrs.5298>.
- [21] M. Verhaegen, S. Lessard, S. Blais-Ouellette, Narrow band SWIR hyperspectral imaging: a new approach based on volume Bragg grating, *Proc. SPIE.* 8374 (2012) 83740G. <https://doi.org/10.1117/12.920811>.
- [22] Certain commercial equipment, instruments, software, or materials are identified in this paper to specify the experimental procedure adequately. Such identification is not intended to imply recommendation or endorsement by the National Institute of Standards and Technology, nor is it intended to imply that the materials or equipment identified are necessarily the best available for the purpose.
- [23] B.H. Hamadani, J. Roller, B. Dougherty, F. Persaud, H.W. Yoon, Absolute spectral responsivity measurements of solar cells by a hybrid optical technique, *Appl. Opt.* 52 (2013) 5184. <https://doi.org/10.1364/AO.52.005184>.
- [24] B.M.F.Y. Jeco, H. Xu, M. Sugiyama, Y. Okada, Luminescence imaging of III-V multijunction solar cells with luminescent coupling effect, in: 2020 47th IEEE Photovolt. Spec. Conf., IEEE, 2020: pp. 0584–0586. <https://doi.org/10.1109/PVSC45281.2020.9300401>.
- [25] J. Jia, Y. Miao, Y. Kang, Y. Huo, M. Mazouchi, Y. Chen, L. Zhao, H. Deng, P. Supaniratisai, S.H. AlQahtani, J.S. Harris, Bias-dependence of luminescent coupling efficiency in multijunction solar cells, *Opt. Express.* 23 (2015) A219. <https://doi.org/10.1364/OE.23.00A219>.
- [26] N. Márquez Peraca, P.M. Haney, B.H. Hamadani, The effect of luminescent coupling on modulated photocurrent measurements in multijunction solar cells, *Appl. Phys. Lett.* 115 (2019) 083506. <https://doi.org/10.1063/1.5115014>.
- [27] ASTM, ASTM E490-00a: Solar constant and zero air mass solar spectral irradiance tables, *Annu. B. ASTM Stand.* 15.03 (2006) 1–16. <https://doi.org/10.1520/E0490-00AR14.2>.
- [28] S.M. Chavali, Characterization of subcells in multijunction solar cells using electroluminescence, University of Maryland, 2020. <https://doi.org/https://doi.org/10.13016/wjwr-5hhv>.
- [29] T. Gershon, B. Shin, N. Bojarczuk, T. Gokmen, S. Lu, S. Guha, Photoluminescence characterization of a high-efficiency Cu₂ZnSnS₄ device, *J. Appl. Phys.* 114 (2013) 154905. <https://doi.org/10.1063/1.4825317>.
- [30] T. Kirchartz, U. Rau, M. Kurth, J. Mattheis, J.H. Werner, Comparative study of electroluminescence from Cu(In,Ga)Se₂ and Si solar cells, *Thin Solid Films.* 515 (2007) 6238–6242. <https://doi.org/10.1016/j.tsf.2006.12.105>.
- [31] O. Dupré, R. Vaillon, M.A. Green, Physics of the temperature coefficients of solar cells, *Sol. Energy Mater. Sol. Cells.* 140 (2015) 92–100. <https://doi.org/10.1016/j.solmat.2015.03.025>.
- [32] B.H. Hamadani, Understanding photovoltaic energy losses under indoor lighting conditions, *Appl. Phys. Lett.* 117 (2020) 043904. <https://doi.org/10.1063/5.0017890>.
- [33] B.M. Kayes, H. Nie, R. Twist, S.G. Spruytte, F. Reinhardt, I.C. Kizilyalli, G.S. Higashi, 27.6% Conversion

efficiency, a new record for single-junction solar cells under 1 sun illumination, in: 2011 37th IEEE Photovolt. Spec. Conf., IEEE, 2011: pp. 000004–000008. <https://doi.org/10.1109/PVSC.2011.6185831>.